

Modelling the Galactic disc: perturbed distribution functions in the presence of spiral arms

Giacomo Monari*, Benoit Famaey, Arnaud Siebert

Observatoire astronomique de Strasbourg, Université de Strasbourg, CNRS UMR 7550, 11 rue de l'Université, 67000 Strasbourg, France

Released 2015 Xxxxx XX

ABSTRACT

Starting from an axisymmetric equilibrium distribution function (DF) in action space, representing a Milky Way thin disc stellar population, we use the linearized Boltzmann equation to explicitly compute the response to a three-dimensional spiral potential in terms of the perturbed DF. This DF, valid away from the main resonances, allows us to investigate a snapshot of the velocity distribution at any given point in three-dimensional configuration space. Moreover, the first order moments of the DF give rise to non-zero radial and vertical bulk flows – namely breathing modes – qualitatively similar to those recently observed in the extended Solar neighbourhood. We show that these analytically predicted mean stellar motions are in agreement with the outcome of test-particle simulations. Moreover, we estimate for the first time the reduction factor for the vertical bulk motions of a stellar population compared to the case of a cold fluid. Such an explicit expression for the full perturbed DF of a thin disc stellar population in the presence of spiral arms will be helpful in order to dynamically interpret the detailed information on the Milky Way disc stellar kinematics that will be provided by upcoming large astrometric and spectroscopic surveys of the Galaxy.

Key words: Galaxy: kinematics and dynamics – Galaxy: disc – Galaxy: solar neighbourhood – Galaxy: structure – Galaxy: evolution – galaxies: spiral

1 INTRODUCTION

The primary objective of the current and future large spectroscopic and astrometric surveys of the Milky Way, culminating with the Gaia mission (Prusti 2012), will be to provide a detailed dynamical model of the Galaxy, including all of its components, and giving us insight into its structure, its formation and its evolutionary history.

The top-down dynamical approach consists in producing *ab initio* simulations of Milky Way-like galaxies in a cosmological context. This approach can be useful to understand some general features of galaxy formation (e.g., Minchev et al. 2014). However, it is not flexible enough to produce an acceptable model for the wide range of extremely detailed data soon to be available for our own Galaxy. On the other side, the bottom-up approach for dynamical modelling consists in starting from the actual Galactic data, rather than from simulations, in order to construct a model of the Galaxy. To avoid the redundancy and computational waste of representing the orbits of every single particle in the model, one can use a phase-space distribution function (DF) to represent each population of constituent particles (typically, various stellar populations and dark matter, see e.g.

Piffl et al. 2015; Binney & Piffl 2015). The model-building generally starts from the assumptions of dynamical equilibrium and axisymmetry. These assumptions allow us to make use of Jeans' theorem constraining the DF to depend only on three integrals of motion, which can typically be chosen to be the radial, azimuthal, and vertical action variables. However, one should remember, especially when modelling the stellar populations of the Galactic disc, that the Galaxy is obviously not axisymmetric, as it harbours a central bar as well as spiral arms. Such perturbations can obviously be treated through perturbation theory, whose foundations in the case of flat 2D discs have been laid down by Kalnajs (1971). For instance, following up on the work of Binney & Lacey (1988) who derived the orbit-averaged Fokker-Planck equation for a 2D stellar disc, recent investigations (e.g., Fouvry et al. 2015) have focused on the long-term secular evolution of such a flat disc by means of diffusion through action-space at resonances, producing ridges in action-space. Here, we are rather interested in the present-day perturbed distribution function in the action-angle space of the unperturbed Hamiltonian, in the presence of a 3D spiral arm perturber, which could be fitted to a snapshot of the Galaxy taken by current and upcoming large surveys. Our philosophy is thus closer to that of McMillan (2013), except that the shape of the perturbed DF will be computed directly from

* Email: giacomo.monari@astro.unistra.fr

the linearized Boltzmann equation. Moreover, in this paper, we will first concentrate only on the response *away* from the main resonances, the extremely interesting effects expected at resonances, as well as the effect of resonance overlaps of multiple perturbers (e.g. Quillen 2003; Minchev & Famaey 2010), being the subject of further analytical work.

One potential issue with assuming axisymmetry in order to produce a benchmark model of the Galaxy from a Galactic survey snapshot is that it is not clear that the fundamental parameters entering the model, such as the peculiar motion of the Sun, will not be biased by forcing the model to fit observed non-axisymmetric features that are not present in the axisymmetric model itself. This could for instance explain why current determinations of the peculiar motion of the Sun are discrepant with each other when using local or non-local tracers (Schönrich et al. 2010; Schönrich 2012). It would thus be extremely useful, especially when modelling the Galactic disc stellar populations, to directly include in the model the response of the stellar DF to the bar or to spiral arms.

In this contribution, we make a step in this direction by analytically investigating the response of a typical stellar population representative of the thin disc of the Galaxy to a 3D perturbing spiral potential. More specifically, we are able to provide the fully explicit form of the perturbed DF in angle-action variables, which could later on be used for dynamical modelling of the disc stellar populations. However, the main problem with including spirals in our model is that the nature and origin of spiral arms in galactic discs are still mostly unknown. Recent numerical investigations indicate that spirals might consist of multiple long-lived (~ 10 galaxy rotations) modes (Sellwood & Carlberg 2014), which do not appear to be strictly static as in the classical density wave picture, but are nevertheless genuine standing wave oscillations with fixed shape and pattern speed. The response to these waves away from the main resonances and the regions where nonlinear coupling between the modes is important can then be computed from perturbation theory, and can in principle be linearly added to each other. Hence, it is interesting to consider the response of the DF to a single such mode, which we will assume here to have non-varying amplitude but which could be later generalized to varying amplitudes too. In the present work, we will concentrate on the response of a given disc stellar population in equilibrium to a perturbing spiral potential in 3D, but we do not investigate yet the conditions for self-consistency.

In Section 2, we recall the basics of action-angle variables and equilibrium distributions functions in action space. The response of a stellar population, represented by a given equilibrium distribution, to a perturbing potential is then presented in Section 3, by means of the linearized collisionless Boltzmann equation. We compute both the perturbed DF and its first order moments, giving the mean stellar motions. The results for the specific case of a spiral perturber are presented in Section 4, and conclusions are drawn in Section 5.

2 EQUILIBRIUM DISTRIBUTION FUNCTIONS IN ACTION SPACE

It is well-known that, in realistic axisymmetric and time-independent Galactic potentials, most orbits are regular (i.e., they are quasiperiodic in the sense that their Fourier transforms have only discrete frequencies that are integer linear combinations of 3 fundamental frequencies) and thus have three isolating integrals of the motion. Each triplet of them specifies a particular orbit in the potential of the Galaxy. Jeans’ theorem then tells us that the equilibrium stellar phase-space DF of any component of the Galaxy, f_0 , should depend only on these three integrals, which makes f_0 automatically a solution of the collisionless Boltzmann equation:

$$\frac{df_0}{dt} = 0. \quad (1)$$

There are in principle an infinity of sets of isolating integrals of the motion to choose from.

On the other hand, if one of the configuration space variables of a dynamical system is absent from the Hamiltonian, then its conjugate momentum is itself an integral of the motion, as is evident from Hamilton’s equations. Conversely, if an integral of the motion has a canonically conjugate variable, the Hamiltonian does not depend on that variable. Hence by choosing three isolating integrals of the motion having canonically conjugate variables, the Hamiltonian can be written in its simplest form, purely as a function of the three integrals of the motion. This makes such a choice of integrals particularly appealing. Such integrals are called the “action variables” \mathbf{J} , and correspond to new generalized momenta. Their canonically conjugate variables are called the “angle variables” $\boldsymbol{\theta}$, because they can be normalized such that the position in phase-space is 2π -periodic in them.

The equations of motion (Hamilton’s equations) are conveniently expressed as

$$\dot{\boldsymbol{\theta}} = \frac{\partial H_0}{\partial \mathbf{J}} = \boldsymbol{\omega}(\mathbf{J}), \quad \dot{\mathbf{J}} = -\frac{\partial H_0}{\partial \boldsymbol{\theta}} = 0. \quad (2)$$

For a star in an axisymmetric disc galaxy, for which the usual phase-space coordinates are the cylindrical coordinates (R, ϕ, z) and their associated velocities $(v_R, v_\phi, v_z) \equiv (\dot{R}, R\dot{\phi}, \dot{z})$, $\mathbf{J} = (J_R, J_\phi, J_z)$ are the actions, $\boldsymbol{\theta} = (\theta_R, \theta_\phi, \theta_z)$ the angles, and $H_0(\mathbf{J})$ is the Hamiltonian corresponding to the axisymmetric time-independent potential Φ_0 . The motion is as simple as one can imagine, since the actions \mathbf{J} are constant in time, and define orbital tori on which the angles just evolve linearly with time, i.e., $\boldsymbol{\theta}(t) = \boldsymbol{\omega}t + \boldsymbol{\theta}_0$, where $\boldsymbol{\omega}(\mathbf{J}) \equiv \partial H_0 / \partial \mathbf{J}$ are the orbital fundamental frequencies.

One of the drawbacks is that we can write analytical relations between the action-angles $(\mathbf{J}, \boldsymbol{\theta})$ and the usual phase-space coordinates (\mathbf{x}, \mathbf{v}) only in some rare cases¹ of poten-

¹ Note that, for any choice of integrals, the third integral cannot, in general, be written analytically for a disc galaxy, apart when the vertical motion is considered separable from the horizontal one as assumed here, or if the potential is of Stäckel form (e.g., Famaey & Dejonghe 2003). Bienaymé et al. (2015) provide typical analytic approximations for the third integral in more realistic potentials, based on the Stäckel approximation, but the corresponding actions are not analytic either.

tials Φ_0 . But the advantages are numerous. First of all, in an equilibrium configuration for the Galaxy, the phase of the stars, θ , are uniformly distributed (phase mixed) on orbital tori specified by \mathbf{J} alone, and the phase-space density of stars $f_0(\mathbf{J})d^3\mathbf{J}$ is just the number of stars dN in a given infinitesimal action range divided by a factor $(2\pi)^3$. Secondly, the actions are adiabatically invariant for a slow secular evolution of the Galactic potential. And finally, they are very natural coordinates for perturbation theory: the linearized collisionless Boltzmann equation takes a rather simple form with these variables (see Section 3).

For simplicity, we are going to work here in the epicyclic and adiabatic approximations (for various more rigorous ways of evaluating the actions, see, e.g., McGill & Binney 1990; McMillan & Binney 2008; Binney & McMillan 2011; Binney 2012; Bovy & Rix 2013; Sanders & Binney 2014), assuming separable motion in the vertical and horizontal directions. The epicyclic approximation is roughly valid for the thin disc we want to model here, i.e. for not too eccentric orbits and close enough to the Galactic plane. It consists in locally approximating the radial and vertical motions of an orbit of angular momentum $L_z \equiv Rv_\phi$ with harmonic motions, i.e., with an effective potential in the meridional plane of the form

$$\Phi_{0,\text{eff}} = \Phi_0 + \frac{L_z}{2R^2} \simeq E_c + \Phi_{0,R} + \Phi_{0,z}, \quad (3)$$

where $\Phi_{0,R} \equiv \kappa^2(R - R_g)^2/2$, $\Phi_{0,z} \equiv \nu^2 z^2/2$, and the radial and vertical epicyclic frequencies, κ and ν , are evaluated at R_g , the radius of a circular orbit of angular momentum L_z , whose energy is E_c . The techniques and results developed in this paper are nevertheless in principle generalizable to more precise and general estimates of the actions for a wider range of orbits, which will be the topic of further papers. Within the adiabatic and epicyclic approximations, the actions (J_R, J_ϕ, J_z) are approximated by the following explicit analytic form:

$$\begin{aligned} J_\phi &= \frac{1}{2\pi} \int_0^{2\pi} d\phi L_z = L_z, \\ J_z &\simeq \frac{1}{\pi} \int_{z_{\min}}^{z_{\max}} dz \sqrt{2[E_z - \Phi_{0,z}]} = \frac{E_z}{\nu}, \\ J_R &\simeq \frac{1}{\pi} \int_{R_{\min}}^{R_{\max}} dR \sqrt{2(E_R - \Phi_{0,R})} = \frac{E_R}{\kappa}, \end{aligned} \quad (4)$$

where $E_R = v_R^2/2 + \kappa^2(R - R_g)^2/2$ is the radial epicyclic energy and $E_z = v_z^2/2 + \nu^2 z^2/2$ is the vertical energy. The canonically conjugate angle variables can then also be expressed explicitly (Dehnen 1999; Binney & Tremaine 2008) as:

$$\begin{aligned} \theta_\phi &\simeq \phi + \Delta\phi, \\ \theta_z &\simeq \tan^{-1} \left(-\frac{v_z}{\nu z} \right), \\ \theta_R &\simeq \tan^{-1} \left(-\frac{v_R}{\kappa(R - R_g)} \right), \end{aligned} \quad (5)$$

where²

$$\Delta\phi \equiv -\frac{\gamma}{R_g} \sqrt{\frac{2J_R}{\kappa}} \sin\theta_R - \frac{J_R}{2} \frac{d \ln \kappa}{dJ_\phi} \sin(2\theta_R), \quad (6)$$

with

$$\gamma \equiv 2\Omega/\kappa, \quad (7)$$

and Ω the angular circular frequency evaluated at $R_g(J_\phi)$. Finally, the orbital frequencies are approximated by

$$\begin{aligned} \omega_\phi &\simeq \Omega + (d\kappa/dJ_\phi)J_R, \\ \omega_z &\simeq \nu, \\ \omega_R &\simeq \kappa. \end{aligned} \quad (8)$$

The possible choices of realistic DFs to represent the different components of the Galactic disc are again numerous (see e.g., Binney 2010; Binney et al. 2014). Here we will make the simplest assumption, i.e. that the axisymmetric thin disc is well represented by a Schwarzschild DF (Binney & Tremaine 2008), i.e.,

$$f_0(J_R, J_\phi, J_z) = \frac{\gamma \tilde{\Sigma}_0 \exp(-R_g/h_R)}{4(2\pi)^{3/2} \tilde{\sigma}_R^2 \tilde{\sigma}_z z_0} \exp\left(-\frac{J_R \kappa}{\tilde{\sigma}_R^2} - \frac{J_z \nu}{\tilde{\sigma}_z^2}\right), \quad (9)$$

where $\tilde{\Sigma}_0$, $\tilde{\sigma}_R$, $\tilde{\sigma}_z$, κ , ν , and γ are all functions of J_ϕ through a chosen dependence on $R_g(J_\phi)$. Note however that most results in Section 3 will be fully independent of this particular choice for f_0 .

3 LINEARIZED COLLISIONLESS BOLTZMANN EQUATION

3.1 General solution

In this section, we will consider a small perturbation to the potential, denoted $\epsilon\Phi_1$ where $\epsilon \ll 1$, Φ_1 has the same order of magnitude as the axisymmetric background potential Φ_0 , and the total potential is $\Phi = \Phi_0 + \epsilon\Phi_1$. Instead of searching for new action-angle variables for the perturbed Hamiltonian $H_1 = H_0 + \epsilon\Phi_1$, we will continue here to work with the variables defined within the *unperturbed* Hamiltonian H_0 . These are obviously no longer action-angle variables within H_1 , but they remain canonical. The following calculations in this Section 3.1 are fully independent from the specific action-angle estimate and choice of DF mentioned at the end of Section 2. We will move to specific predictions involving our specific choice of variables only in Section 3.2.

With such a perturbation, the DF becomes, to first order in ϵ , $f = f_0 + \epsilon f_1$, which should still be a solution of the collisionless Boltzmann equation, Eq. (1). To first order in ϵ (i.e. dropping higher-order terms), this leads to the *linearized* collisionless Boltzmann equation, which reads (Eqs. 5.13 & 5.14 of Binney & Tremaine 2008):

$$\frac{df_1}{dt} + [f_0, \Phi_1] = 0, \quad (10)$$

² Rigorously speaking θ_ϕ , the canonical conjugate of J_ϕ , should also include a term dependent on the vertical motion $-J_z(d \ln \nu/dJ_\phi) \cos\theta_z \sin\theta_z$ which in typical thin disc situations is tiny, much smaller than the already small $-J_R(d \ln \kappa/dJ_\phi) \sin(2\theta_R)$, and which therefore we omit.

where the time-derivative of f_1 is a *total* derivative and $[f_0, \Phi_1]$ is the Poisson bracket estimated along the unperturbed orbits. It thus appears immediately that for a given axisymmetric equilibrium DF, f_0 , and a given perturbing potential, Φ_1 , the response f_1 can be computed.

Integrating Eq. (10) within angle-action coordinates leads to

$$f_1(\mathbf{J}, \boldsymbol{\theta}, t) = \int_{-\infty}^t dt' \frac{\partial f_0}{\partial \mathbf{J}'}(\mathbf{J}') \cdot \frac{\partial \Phi_1}{\partial \boldsymbol{\theta}'}(\mathbf{J}', \boldsymbol{\theta}', t'), \quad (11)$$

where the coordinates $(\mathbf{J}', \boldsymbol{\theta}')$ correspond to the orbits in the unperturbed potential. Note that the perturbing potential Φ_1 is assumed to have an explicit dependence on time.

Since the angle variables are defined such that the position in phase-space is 2π -periodic in them, we consider only cases where Φ_1 is cyclic in the angle coordinates, i.e.,

$$\Phi_1|_{\theta_i} = \Phi_1|_{\theta_i + 2\pi}, \quad (12)$$

where θ_i is any of the angle coordinates and the vertical line means that Φ_1 is evaluated keeping constant all the other variables. Then, Φ_1 can be expanded in a Fourier series as

$$\Phi_1(\mathbf{J}, \boldsymbol{\theta}, t) = \text{Re} \left\{ \mathcal{G}(t) \sum_{\mathbf{n}} c_{\mathbf{n}}(\mathbf{J}) e^{i\mathbf{n} \cdot \boldsymbol{\theta}} \right\}, \quad (13)$$

where $\mathcal{G}(t)$ controls the strength of the perturbation as a function of time. It is convenient to factorize this function into two factors, $\mathcal{G}(t) = g(t)h(t)$, where $g(t)$ is a well behaved function controlling the general amplitude of the perturbation, and $h(t)$ is a periodic sinusoidal function of frequency ω_p , which can account for a perturbing potential rotating with a fixed pattern speed. Hereabove, \mathbf{n} is a triple of indexes running from $-\infty$ to ∞ . Then Eq. (11) becomes

$$f_1(\mathbf{J}, \boldsymbol{\theta}, t) = \text{Re} \left\{ i \frac{\partial f_0}{\partial \mathbf{J}}(\mathbf{J}) \cdot \sum_{\mathbf{n}} \mathbf{n} c_{\mathbf{n}}(\mathbf{J}) \times \int_{-\infty}^t dt' g(t') h(t') e^{i\mathbf{n} \cdot \boldsymbol{\theta}'(t')} \right\}. \quad (14)$$

Integrating by parts, the solution of the integral in Eq. (14) is

$$\int_{-\infty}^t dt' g(t') h(t') e^{i\mathbf{n} \cdot \boldsymbol{\theta}'(t')} = \sum_{k=0}^{\infty} \left[(-1)^k \frac{h(t') e^{i\mathbf{n} \cdot \boldsymbol{\theta}'(t')} g^{(k)}(t')}{(i\mathbf{n} \cdot \boldsymbol{\omega} + i\omega_p)^{k+1}} \right]_{-\infty}^t. \quad (15)$$

We assume that the perturbation and its time derivatives are null far back in time, i.e., $g^{(k)}(-\infty) = 0$. Moreover, we assume in the following that the amplitude of the perturbation is constant at the present time t , hence $g^{(0)}(t) = 1$, and $g^{(k)}(t) = 0$, for $k = 1, \dots, \infty$. This finally leads to

$$f_1(\mathbf{J}, \boldsymbol{\theta}, t) = \text{Re} \left\{ \frac{\partial f_0}{\partial \mathbf{J}}(\mathbf{J}) \cdot \sum_{\mathbf{n}} \mathbf{n} c_{\mathbf{n}}(\mathbf{J}) \frac{h(t) e^{i\mathbf{n} \cdot \boldsymbol{\theta}}}{\mathbf{n} \cdot \boldsymbol{\omega} + \omega_p} \right\}. \quad (16)$$

Within the above assumption of a currently non-varying amplitude of the perturbation, this solution is completely general and independent of any choice of action-angle coordinates and of any choice of a particular form of the axisymmetric equilibrium DF f_0 . Note that Carlberg & Sellwood (1985) and Carlberg (1987) have on their side investigated

the lasting changes in the distribution function after a transient spiral has come and gone. While similar in spirit to the present work, the goal was very different and needed to consider the second-order response, since to first-order, after the spiral has vanished, the DF goes back to its initial state through phase-mixing. Our approach is rather approximating what happens when the amplitude of the spiral wave reaches a plateau at its maximum.

3.2 Fourier modes perturbing potential within the epicyclic approximation

To be more specific, we now consider a perturbing potential of the form

$$\Phi_1(R, \phi, z, t) = \text{Re} \left\{ \Phi_a(R, z) e^{im(\phi - \Omega_p t)} \right\}, \quad (17)$$

i.e., a pure Fourier mode in ϕ , which is a good approximation for the potential of a given spiral arm mode, or the bar (at least away from the center of the Galaxy). Note that we only consider hereafter plane-symmetric potentials $\Phi_a(R, |z|)$, thereby not addressing perturbations such as corrugation waves. Here, Ω_p is simply the pattern speed, while m is the azimuthal wavenumber (e.g., $m = 2$ for the bar or a 2-armed spiral, $m = 4$ for a 4-armed spiral).

At this point, in order to specify the above solution f_1 (Eq. 16) within that perturbing potential, we have to rewrite Φ_1 as in Eq. (13). To do so, we approximate $\Phi_a(R, z)$ close to the plane as

$$\Phi_a(R, z) \approx \Phi_a(R, 0) + \frac{1}{2} \frac{\partial^2 \Phi_a}{\partial z^2}(R, 0) z^2, \quad (18)$$

which is valid in the same range of z as the epicyclic approximation. So, Φ_1 becomes

$$\Phi_1 \approx \Phi_{1,R}(R, \phi) + \Phi_{1,z}(R, \phi, z), \quad (19)$$

where

$$\begin{aligned} \Phi_{1,R} &\equiv \text{Re} \left\{ \Phi_a(R, 0) e^{im(\phi - \Omega_p t)} \right\}, \\ \Phi_{1,z} &\equiv \text{Re} \left\{ \frac{\partial^2 \Phi_a(R, 0)}{\partial z^2} \frac{z^2}{2} e^{im(\phi - \Omega_p t)} \right\}. \end{aligned} \quad (20)$$

We start with $\Phi_{1,R}$. The radial motion in the epicyclic approximation is written

$$R = R_g (1 - e) \cos \theta_R, \quad (21)$$

where

$$e(J_R, J_\phi) \equiv \sqrt{2J_R / (\kappa R_g^2)} \quad (22)$$

is the eccentricity of the orbit. We consider orbits with low e , for which the epicyclic approximation holds. Using the definition of e and the mapping of Eq. (4) and Eq. (5), we can rewrite $\Phi_{1,R}$ and expand it in powers of e , dropping all the terms that are $O(e^2)$, to obtain (e.g., Weinberg 1994)

$$\begin{aligned} \Phi_{1,R} &= \text{Re} \left\{ \Phi_a(R, 0) e^{im(\theta_\phi - \Delta\phi - \Omega_p t)} \right\} \\ &\approx \text{Re} \left\{ \left[\Phi_a(R_g, 0) (1 + im e \gamma \sin \theta_R) + \right. \right. \\ &\quad \left. \left. - \frac{\partial \Phi_a}{\partial R}(R_g, 0) e \cos \theta_R \right] e^{im(\theta_\phi - \Omega_p t)} \right\}, \end{aligned} \quad (23)$$

where γ is defined as in Eq. (7). Note that the function

$h(t)$ in Eq. (13) is just $h(t) = \exp(-im\Omega_p t)$ in this case, and the frequency ω_p in Eqs. (15)-(16) is thus $\omega_p = -m\Omega_p$. We can now evaluate the Fourier coefficients for $\Phi_{1,R}$ in the traditional way

$$\begin{aligned} c_{jkl}^R(J_R, J_\phi, J_z) &= \frac{1}{(2\pi)^3} \int_0^{2\pi} d\theta_R \int_0^{2\pi} d\theta_\phi \\ &\times \int_0^{2\pi} d\theta_z \Phi_a(R, 0) e^{im(\theta_\phi - \Delta\phi)} e^{-i(j\theta_R + k\theta_\phi + l\theta_z)} \\ &\approx \delta_{km} \delta_{l0} \left\{ \left[\delta_{j0} + \delta_{|j|1} \frac{k}{2} \text{sgn}(j) \gamma e \right] \Phi_a(R_g, 0) \right. \\ &\quad \left. - \delta_{|j|1} \frac{R_g}{2} e \frac{\partial \Phi_a}{\partial R}(R_g, 0) \right\}, \end{aligned} \quad (24)$$

where δ is the Kronecker delta. We can now also treat $\Phi_{1,z}$ in the same way, replacing $\Phi_a(R, 0)$ herabove by $\frac{\partial^2 \Phi_a(R, 0)}{\partial z^2} \frac{z^2}{2}$. From Eq. (5), we note that z^2 can be expressed as

$$z^2 = \frac{2J_z}{\nu} \cos^2 \theta_z = \frac{J_z}{\nu} \sum_{l=-1}^1 \frac{e^{i2l\theta_z}}{2^{|l|}}. \quad (25)$$

The Fourier coefficients for $\Phi_{1,z}$ are then

$$\begin{aligned} c_{jkl}^z(J_R, J_\phi, J_z) &= \frac{1}{(2\pi)^3} \int_0^{2\pi} d\theta_R \int_0^{2\pi} d\theta_\phi \\ &\times \int_0^{2\pi} d\theta_z \frac{\partial^2 \Phi_a(R, 0)}{\partial z^2} \frac{z^2}{2} e^{im(\theta_\phi - \Delta\phi)} e^{-i(j\theta_R + k\theta_\phi + l\theta_z)} \\ &\approx \frac{1}{2} \delta_{km} \left(\delta_{l0} + \frac{\delta_{|l|2}}{2} \right) \frac{J_z}{\nu} \left\{ \left[\delta_{j0} + \delta_{|j|1} \frac{k}{2} \text{sgn}(j) \gamma e \right] \right. \\ &\quad \left. \times \frac{\partial^2 \Phi_a}{\partial z^2}(R_g, 0) - \delta_{|j|1} \frac{R_g}{2} e \frac{\partial^3 \Phi_a}{\partial R \partial z^2}(R_g, 0) \right\}. \end{aligned} \quad (26)$$

We can now rewrite f_1 (Eq. 16) as

$$f_1 = f_{1,R} + f_{1,z}, \quad (27)$$

where

$$f_{1,R} \equiv \text{Re} \left\{ \sum_{j=-1}^1 c_{jm0}^R F_{jm0} e^{i[j\theta_R + m(\theta_\phi - \Omega_p t)]} \right\}, \quad (28)$$

$$f_{1,z} \equiv \text{Re} \left\{ \sum_{j,l=-1}^1 c_{jm2l}^z F_{jm2l} e^{i[j\theta_R + m(\theta_\phi - \Omega_p t) + 2l\theta_z]} \right\}, \quad (29)$$

where the Fourier coefficients c_{jkl}^R and c_{jkl}^z are given by Eq. (24), Eq. (26), and

$$F_{jkl}(J_R, J_\phi, J_z) \equiv \frac{j \frac{\partial f_0}{\partial J_R} + k \frac{\partial f_0}{\partial J_\phi} + l \frac{\partial f_0}{\partial J_z}}{j\kappa + k(\omega_\phi - \Omega_p) + l\nu}. \quad (30)$$

3.3 Moments of the distribution function

One of the main motivation of the present work is to understand the present response of a disc stellar population, represented by a DF f_0 in an axisymmetric potential, to a quasi-static perturbing non-axisymmetric potential in terms of radial and vertical mean motions (e.g., Faure et al. 2014). Such mean motions can be computed through the zeroth and first order moments of the perturbed DF $f = f_0 + \epsilon f_1$. Here

we will assume a given form for f_0 , namely the Schwarzschild DF of Eq. (9).

We will focus on the mean motions projected on the plane (for the radial motion) and on both sides of the plane (for the vertical motion). Indeed, it was already shown numerically (Faure et al. 2014; Monari et al. 2015) that spiral or bar perturbations typically lead to a *breathing mode* response of the disc, i.e. a density response that has even parity with respect to the Galactic plane (i.e., is plane-symmetric), and a mean vertical velocity field that has odd parity. Hence we will concentrate hereafter on the projected surface density $\Sigma(R, \phi)$, the projected mean radial velocity field $\langle v_R \rangle(R, \phi)$, and the difference between the mean vertical velocity field above and below the plane

$$\Delta \langle v_z \rangle(R, \phi) \equiv \langle v_z \rangle(z > 0) - \langle v_z \rangle(z < 0). \quad (31)$$

These can be computed by integrating the perturbed DF over all z (or half of them in the case of the vertical motion) and all velocities, i.e.,

$$\Sigma(R, \phi) \equiv \int_{-\infty}^{\infty} dz \int d^3 \mathbf{v} (f_0 + \epsilon f_1), \quad (32a)$$

$$\Sigma(R, \phi) \langle v_R \rangle(R, \phi) \equiv \int_{-\infty}^{\infty} dz \int d^3 \mathbf{v} v_R (f_0 + \epsilon f_1), \quad (32b)$$

$$\Sigma(R, \phi) \Delta \langle v_z \rangle(R, \phi) \equiv 4 \int_0^{\infty} dz \int d^3 \mathbf{v} v_z (f_0 + \epsilon f_1), \quad (32c)$$

where

$$d^3 \mathbf{v} = dv_\phi dv_R dv_z. \quad (33)$$

Note that, by integrating over half of the z for $\Delta \langle v_z \rangle$, we get only half of the surface density, and have to multiply by two again to get the subtraction between the mean vertical velocities above and below the plane, hence the factor of four. Now, using the parity of the functions, Eq. (32) simplify to

$$\Sigma(R, \phi) = \int_{-\infty}^{\infty} dz \int d^3 \mathbf{v} (f_0 + \epsilon f_1), \quad (34a)$$

$$\Sigma(R, \phi) \langle v_R \rangle(R, \phi) = \epsilon \int_{-\infty}^{\infty} dz \int d^3 \mathbf{v} v_R f_1, \quad (34b)$$

$$\Sigma(R, \phi) \Delta \langle v_z \rangle(R, \phi) = 4\epsilon \int_0^{\infty} dz \int d^3 \mathbf{v} v_z f_{1,z}. \quad (34c)$$

These integrals have to be solved at constant (R, ϕ, t) . To compute the integrals over all velocities, we pass from the integration coordinates (v_R, v_ϕ, v_z) (where v_R and v_z range from $-\infty$ to ∞ , and v_ϕ from 0 to ∞) to $(\theta_R, \theta_z, J_\phi)$ (where θ_R and θ_z range from $-\pi/2$ to $\pi/2$, and J_ϕ from 0 to ∞) via the transformations

$$v_R = -\kappa(R - R_g) \tan \theta_R, \quad (35a)$$

$$v_\phi = J_\phi / R, \quad (35b)$$

$$v_z = -\nu z \tan \theta_z, \quad (35c)$$

and

$$J_R = \frac{(R - R_g)^2 \kappa}{2 \cos^2 \theta_R}, \quad (36a)$$

$$J_z = \frac{z^2 \nu}{2 \cos^2 \theta_z}, \quad (36b)$$

$$\theta_\phi = \phi + \Delta\phi(\theta_R). \quad (36c)$$

The Jacobian of the transformation is

$$dv_R dv_\phi dv_z = \frac{\kappa\nu(R - R_g)z}{R \cos^2 \theta_R \cos^2 \theta_z} d\theta_R d\theta_z dJ_\phi, \quad (37)$$

Using these transformations, as well as the approximations $\omega_\phi \approx \Omega$, $\exp(im\Delta\phi) \approx (1 + im\Delta\phi)$, $\Delta\phi \approx -\gamma/R_g \sqrt{2J_R/\kappa} \sin\theta_R$ (i.e., up to the first order in e), we compute the integrals of Eq. (34), and the DF f_0 of Eq. (9), to obtain³

$$\Sigma = \Sigma_0 + \epsilon\Sigma_1, \quad (38a)$$

where

$$\Sigma_0 = \frac{(2\pi)^{3/2}}{R} \int_0^\infty dJ_\phi \frac{\tilde{\sigma}_R \tilde{\sigma}_z^2}{\nu} e^{\frac{\psi_R}{\tilde{\sigma}_R^2}} f_0(0, J_\phi, 0), \quad (38b)$$

$$\Sigma_1 = \text{Re} \left\{ \frac{(2\pi)^{3/2} e^{i\hat{\phi}}}{R} \sum_{j=-1}^1 \int_0^\infty dJ_\phi \frac{\tilde{\sigma}_z}{\nu} e^{\frac{\psi_R}{\tilde{\sigma}_R^2}} \left(\hat{\Sigma}_j + \hat{\Sigma}'_{j0} \right) \times \left[\delta_{j0} - \delta_{|j|1} \left(\delta_R - j \frac{m\gamma \tilde{\sigma}_R^2}{\kappa^2 R_g^2} \right) \right] \right\}. \quad (38c)$$

For the mean radial velocity, we get

$$\Sigma \langle v_R \rangle = \text{Re} \left\{ -i\epsilon \frac{(2\pi)^{3/2} e^{i\hat{\phi}}}{R} \sum_{j=-1}^1 \int_0^\infty dJ_\phi \frac{\tilde{\sigma}_z \tilde{\sigma}_R^2}{\nu \kappa R_g} e^{\frac{\psi_R}{\tilde{\sigma}_R^2}} \times \left(\hat{\Sigma}_j + \hat{\Sigma}'_{j0} \right) \left[\delta_{j0} m\gamma - \delta_{|j|1} (j + m\gamma \delta_R) \right] \right\}. \quad (39)$$

Finally, for the difference of mean vertical velocities above and below the plane, we get

$$\Sigma \Delta \langle v_z \rangle = \text{Re} \left\{ -i\epsilon \frac{8\pi e^{i\hat{\phi}}}{R} \sum_{j=-1}^1 \sum_{l=-1}^1 \int_0^\infty dJ_\phi \frac{\tilde{\sigma}_z^2}{\nu} e^{\frac{\psi_R}{\tilde{\sigma}_R^2}} \frac{l}{2^{|l|}} \times \hat{\Sigma}'_{j2l} \left[\delta_{j0} m\gamma - \delta_{|j|1} \left(\delta_R - j m\gamma \frac{\tilde{\sigma}_R^2}{\kappa^2 R_g^2} \right) \right] \right\}, \quad (40)$$

where

$$\delta_R \equiv \frac{R - R_g}{R_g}, \quad (41a)$$

$$\hat{\phi} \equiv m(\phi - \Omega_p t), \quad (41b)$$

$$\psi_R \equiv -\frac{\kappa^2 (R - R_g)^2}{2} \quad (41c)$$

$$\hat{\Sigma}_j \equiv \tilde{\sigma}_R \tilde{\sigma}_z c_{j m 0}^R \left(\frac{\kappa^2 R_g}{2}, J_\phi, 0 \right) F_{j m 0} (0, J_\phi, 0), \quad (41d)$$

$$\hat{\Sigma}'_{jl} \equiv \tilde{\sigma}_R \tilde{\sigma}_z c_{j m l}^R \left(\frac{\kappa^2 R_g}{2}, J_\phi, \frac{\tilde{\sigma}_z^2}{\nu} \right) F_{j m l} (0, J_\phi, 0). \quad (41e)$$

The mean vertical stellar motion is thus non-zero because the factor $\hat{\Sigma}'_{j2l}$ is not the same for $l = 1$ and $l = -1$ in the integrand of Eq. (40).

4 RESULTS

4.1 Spiral arm model

We now wish to obtain explicit results in the case of a given 3D spiral arm perturbation of the Galactic potential. The

parameters of the axisymmetric Galactic potential Φ_0 , the equilibrium DF f_0 , and the spiral perturbation Φ_1 can all be varied in order to get different responses for different parameters, and they could all be used as free parameters when fitting a distribution function to observed stellar kinematics from large Galactic surveys. Here we fix these parameters in order to illustrate the typical behavior of f_1 .

For $\Phi_0(R, z)$, we choose a realistic potential for the Galaxy, namely the Model I of Binney & Tremaine (2008), fitting several observed properties of the Milky Way (see also Dehnen & Binney 1998). It has a spheroidal dark halo and bulge, as well as three components for the disc potential: thin, thick, and ISM disc. The disc densities decrease exponentially with both Galactocentric radius and height from the Galactic plane.

For $f_0(J_R, J_\phi, J_z)$, we choose the Schwarzschild DF of Eq. (9) with $h_R = 2$ kpc, $z_0 = 0.3$ kpc, and

$$\tilde{\sigma}_R(R) = \tilde{\sigma}_R(R_0) e^{-\frac{R-R_0}{5h_R}}, \quad (42a)$$

$$\tilde{\sigma}_z(R) = \tilde{\sigma}_z(R_0) e^{-\frac{R-R_0}{5h_R}}, \quad (42b)$$

where $\tilde{\sigma}_R(R_0) = 35$ km s⁻¹, and $\tilde{\sigma}_z(R_0) = 15$ km s⁻¹.

As a perturbation $\Phi_1(R, z, \phi, t)$ we wish to use a tightly-wound logarithmic spiral. Expressing an analytic potential-density pair for a 3D spiral is not trivial. For instance, if we consider a logarithmic spiral with radial wavenumber $k(R) = m/(R \tan p)$, where p is the pitch angle, one could multiply the 2D potential by $\exp(-|kz|)$, but this would have the drawback that the vertical force field would be discontinuous in the plane. Instead, we use here the spiral arms potential-density pair of Cox & Gómez (2002), which closely resembles arms with a sech² vertical fall-off. With this potential-density pair, our $\Phi_a(R, z)$ in Eq. (12) corresponds to a logarithmic spiral with radially-varying amplitude and radially-varying scale-height, which reads

$$\epsilon\Phi_a(R, z) = -\frac{A}{KD} e^{im[-\phi_s + \frac{\ln(R/R_s)}{\tan p}]} \left[\text{sech} \left(\frac{Kz}{\beta} \right) \right]^\beta, \quad (43)$$

where

$$K(R) = \frac{2}{R \sin p}, \quad (44a)$$

$$\beta(R) = K(R) h_s [1 + 0.4K(R) h_s], \quad (44b)$$

$$D(R) = \frac{1 + K(R) h_s + 0.3 [K(R) h_s]^2}{1 + 0.3K(R) h_s}. \quad (44c)$$

For the length and height parameters of this spiral potential, we choose $R_s = 1$ kpc and $h_s = 0.1$ kpc. We also fix a phase $\phi_s = -26^\circ$ and consider our following results at present time $t = 0$. The spiral is chosen to be tightly-wound with $p = -9.9^\circ$, and the amplitude parameter is chosen to be $A = 683.7$ km² s⁻². Finally, we choose to consider a 2-armed spiral with $\Omega_p = 18.9$ km s⁻¹ kpc⁻¹, so that the main resonances are relatively away from the Solar neighbourhood. The inner Lindblad resonance would be hidden in the central bar region of the Galaxy (ILR = 1.56 kpc) and the corotation is in the outer galaxy (CR = 11.49 kpc). These parameters have been partly inspired by the 2D spiral potential considered in Siebert et al. (2012), and produce at $(R, z) = (8$ kpc, 0) a maximum radial force of the spiral that is 1% of the force due to the axisymmetric background.

With this form of the background potential, axisym-

³ Actually, the explicit results of Eqs. (38)-(40) are valid not only for the Schwarzschild DF of Eq. (9) but for any DF that has a dependence on J_R and J_z of the form $\exp\left(-\frac{J_R \kappa}{\tilde{\sigma}_R^2} - \frac{J_z \nu}{\tilde{\sigma}_z^2}\right)$.

metric equilibrium distribution function, and spiral potential, we can now compute the Fourier coefficients of Eqs. (24) and (26), as well as the perturbed distribution function of Eq. (27) and its moments of Eqs. (38)-(40).

4.2 Moments of the distribution function

4.2.1 Radial velocity gradient

We first consider the integrals in Eqs. (38)-(39), which have to be computed numerically. In practice, for a given R , the integral on J_ϕ is computed in the interval of angular momenta corresponding to circular orbits at the radii where the circular velocity is $v_c \pm 2\bar{\sigma}_R$ (we tested that the results obtained in this way are stable on larger integration ranges). The moments are actually Fourier modes themselves, i.e., they have the form $q(R, \phi) = \text{Re}\{q_a(R) \exp(i\hat{\phi})\}$ where $\hat{\phi}$ is defined as in Eq. (41b). We evaluate $q_a(R)$ numerically on a grid of R values between 1 and 10 kpc with a step 0.25 kpc, and use a 3rd order polynomial interpolation on this grid to obtain the value $q_a(R)$ at a generic R point.

In Fig. 1 we plot Σ_1/Σ_0 and $\Sigma\langle v_R \rangle/\Sigma_0$ as obtained from Eqs. (38)-(40). As we see, the maxima of the response density wake Σ_1/Σ_0 closely follow the loci of the spiral arm potential (dashed red curves), as one expects. On the other hand, stars on the arms tend to move towards the center of the Galaxy ($\langle v_R \rangle < 0$), while those in the interarm regions tend to move outside ($\langle v_R \rangle > 0$).

In order to illustrate how our analytic calculations allow to physically interpret the outcome of simulations, we compare the moments induced by the perturbation derived analytically with those computed with a numerical test-particle simulation. The initial conditions are drawn from f_0 , and with the same potential $\Phi_0 + \epsilon\Phi_1$ (where Φ_1 grows slowly with time, until it reaches the final amplitude used for the analytical predictions). The details of this simulation can be found in Monari et al. (2015), where the only difference with the present simulations is that, in that previous work, Φ_1 was a bar potential instead of the spiral arms that we use here. The results of this simulation are depicted in Fig. 1. We find a very good agreement between the position of the maxima and minima of the moments and the loci of the spiral arms. Moreover, the amplitude of the perturbed density and motions appear to be similar to the analytical predictions. A closer look to this comparison with the simulation is presented in Fig. 2. Here the comparison is made at three different radii, in the neighborhood of $R_0 = 8$ kpc: $R = 7$ kpc, $R = 8$ kpc, and $R = 9$ kpc. These plots confirm the agreement between the simulation and the analytical predictions. Some small discrepancies are of course present, and are due to a combination of different effects. One of them is the discrete nature of the simulations, and the fact that they never reach complete phase-mixing. The second is that, although the area covered is away from the ILR and CR, there still are non-linear effects due to the resonances of higher order than the Lindblad resonances that our analytical method does not describe (e.g., due to the 4 : 1 inner ultra-harmonic resonance between $\Omega - \Omega_p$ and κ , which in our case falls at $R = 7.61$ kpc). The third is the presence of very eccentric orbits, especially in the inner regions of the Galaxy, while Eqs. (38)-(39) are valid only for moderate eccentricities.

All this is especially interesting in view of the large-

scale radial velocity gradient first observed in the Galaxy by Siebert et al. (2011) with the RAVE survey. This was interpreted as the possible effect of either a $m = 2$ spiral (Siebert et al. 2012) or the Galactic bar (Monari et al. 2014). In this respect, it is interesting to note that the amplitude of the radial velocity fluctuations generated by our spiral potential here are of the same order of magnitude as those observed. It should however be noted that subsequently observed large-scale line-of-sight velocity fluctuations with a few red clump stars from the APOGEE survey seem to be more compatible with the effect of the bar Bovy et al. (2015); Grand et al. (2015).

In Siebert et al. (2012), a comparison between the RAVE data and various spiral models was made by using the traditional *reduction factor* \mathcal{F} of Lin & Shu (1964, 1966); Lin et al. (1969) – see also Binney & Tremaine (2008). In the case of a cold, pressureless fluid it can indeed be shown that the linear response to a non-axisymmetric rotating density perturbation $\epsilon\Phi_1$ in the radial velocity on the Galactic plane is

$$\epsilon u_{R,1}(R, \phi) = \text{Re} \left\{ u_R^a(R) e^{im(\phi - \Omega_p t)} \right\}, \quad (45)$$

where

$$u_R^a(R) = i \frac{m}{\Delta(R)} \left\{ [\Omega_p - \Omega(R)] \frac{d\Phi_a}{dR}(R, 0) - \frac{2\Omega(R)\Phi_a(R, 0)}{R} \right\}, \quad (46)$$

and $\Delta(R) \equiv \kappa(R)^2 - m^2 [\Omega_p - \Omega(R)]^2$. When the perturbing potential is a tightly wound spiral, the second term in the r.h.s. of Eq. (46) is much smaller than the first term, and can be omitted, so that Eq. (46) simplifies to

$$u_R^a(R) \approx i \frac{m [\Omega_p - \Omega(R)]}{\Delta(R)} \frac{d\Phi_a}{dR}(R, 0). \quad (47)$$

Lin & Shu (1964, 1966); Lin et al. (1969) offer a way to rewrite Eq. (47) in the case of a stellar disc, i.e., by multiplying it by a reduction factor \mathcal{F} whose derivation is reported in Appendix K of Binney & Tremaine (2008). In Fig. 3 we compare all these predictions with the Eq. (39) of this work and the outcome of our numerical simulations at $R = R_0$. Since \mathcal{F} was derived for tightly wound spirals only, we use the best fit tightly wound spiral potential with the same pitch angle p to $\epsilon\Phi_1$ of this work in the range of R , $6 \text{ kpc} < R < 8 \text{ kpc}$ (left panel), $7 \text{ kpc} < R < 9 \text{ kpc}$ (central panel), and $8 \text{ kpc} < R < 10 \text{ kpc}$ (right panel). We notice that there is a noticeable difference in the amplitude predicted by the Lin-Shu approximation, even with the reduction factor, (a factor ~ 2 or more), and the results obtained using Eq. (39) of the present work: the latter case actually describes much better the numerical simulation, calling for a re-investigation of non-axisymmetric kinematic features in future surveys with our present DF-based method rather than a simple reduction factor. There are several likely reasons for this difference. First of all, our approach is three-dimensional, and takes explicitly into account the vertical velocity dispersion of stars in the response to the perturbation. Second, we do not neglect the tangential force term which is usually neglected for tightly-wound spirals. Third, we use the guiding radius to evaluate our quantities instead of the present position which is used as a proxy in the Lin-Shu approach. Finally, the Lin-Shu approach assumes for the time-variation of the azimuthal angle that of a circular

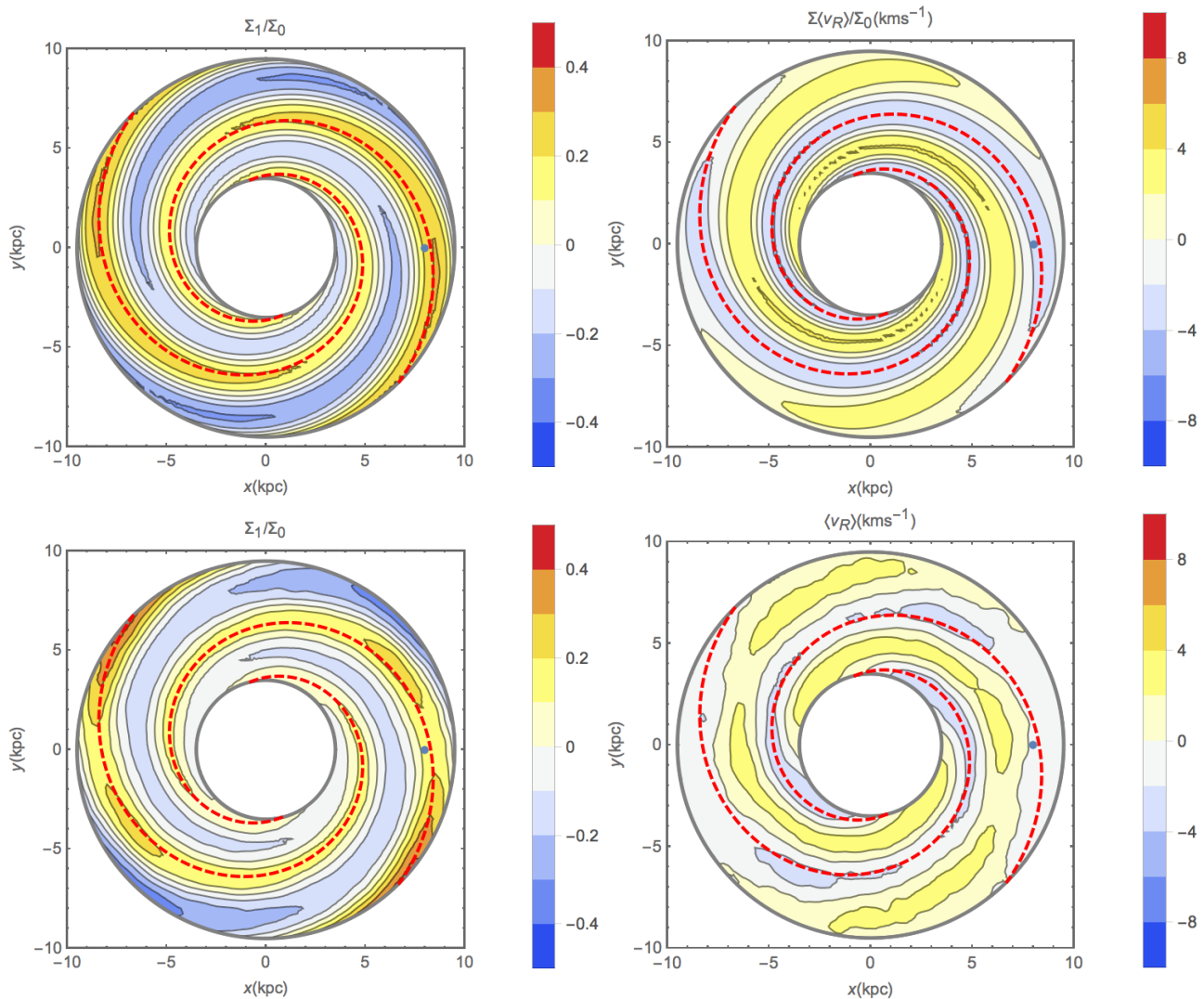


Figure 1. Moments induced by the potential perturbation Eq. (43) on the Binney & Tremaine (2008) Model I potential. Top left: density wake Σ_1/Σ_0 obtained from Eq. (38). Top right: average radial speed $\Sigma\langle v_R \rangle/\Sigma_0$ obtained from Eq. (39). Bottom left: density wake Σ_1/Σ_0 obtained from the simulation. Bottom right: average radial speed $\langle v_R \rangle$ obtained from the simulation. Σ_0 is computed in the simulation averaging Σ over ϕ at a certain R . The dashed red curves represent the loci of the arms.

orbit, which is a good approximation only for very small eccentricities. It is a combination of these effects which leads to the present difference with the Lin-Shu reduction factor.

4.2.2 Vertical bulk motions: breathing mode of the disc

One of the immense advantages of working with a 3D spiral model is that it allows us to investigate the effect of the spiral on mean stellar *vertical* motions. This is especially interesting given that recent Milky Way large spectroscopic surveys have consistently indicated that the mean vertical motion of stars above and below the plane was typically non-zero (Widrow et al. 2012; Williams et al. 2013; Carlin et al. 2013). Such a behaviour was originally associated uniquely with external excitations of the disc by a passing satellite galaxy or a dark matter substructure (Widrow et al. 2012; Gómez et al. 2013; Yanny & Gardner 2013; Feldmann & Spolyar 2015). It is however useful to separate such stel-

lar bulk motions into two types of vertical oscillations. If the density perturbation has odd parity with respect to the Galactic plane, and the vertical velocity field has even parity, the disc itself is subject to a corrugation pattern which is called a “bending mode”. These are indeed mostly caused by external perturbers (Xu et al. 2015; de la Vega et al. 2015; Gómez et al. 2015). On the other hand, if the density wake has even parity while the vertical velocity field has odd parity (i.e., a rarefaction-compression pattern), the oscillation is called a “breathing mode”. Such breathing modes have been shown through test-particle simulations and approximate analytical considerations to be natural consequences of internal non-axisymmetries such as the bar and spiral arms (Faure et al. 2014; Monari et al. 2015). The same effect was also found in self-consistent simulations of isolated galaxies developing spiral instabilities (Debatista 2014). It was even shown that the breathing mode present in the simulation of a Milky Way like galaxy bombarded by satellites, which was analyzed by Widrow et al. (2014), was actually most proba-

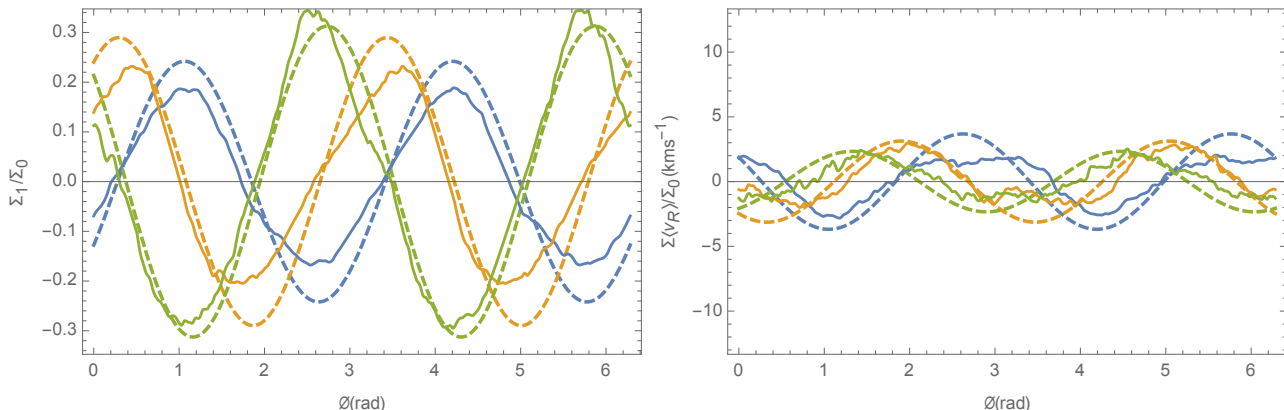


Figure 2. Comparison between the moments induced by the potential perturbation Eq. (43) on the Binney & Tremaine (2008) Model I potential as a function of ϕ at three different radii computed with a numerical test-particle simulation (solid lines) and Eqs. (38)-(39) (dashed lines). Left panel: Σ_1/Σ_0 . Right panel: $\langle v_R \rangle$. Blue lines: $R = 7$ kpc. Orange lines: $R = 8$ kpc. Green lines: $R = 9$ kpc. The moments of the simulation are computed inside $x - y$ square bins of 0.25 kpc side, smoothed with a Gaussian filter on a scale of 0.5 kpc, and polynomial interpolated on the $x - y$ grid.

bly linked to the bar formation rather than induced by the satellites themselves (Monari et al. 2015).

Our present analytic calculations allow for the first time a rigorous and fully dynamical understanding of spiral-induced breathing modes away from the main resonances (and in the absence of resonance overlaps of multiple patterns, which will be the topic of further work). For this, it suffices to integrate Eq. (40) in a similar manner as Eq. (39). The resulting $\Sigma \Delta \langle v_z \rangle / \Sigma_0$ is plotted on Fig. 4. As can be seen, stars tend to vertically move away from the Galactic plane at the outer edge of spiral arms ($\Delta \langle v_z \rangle > 0$) and towards the plane at the inner edge ($\Delta \langle v_z \rangle < 0$), with a clear phase-shift w.r.t. the mean radial motion, already noted in Faure et al. (2014). Again, we compare this to the results of our test-particle simulation (Fig. 4 and Fig. 5) and find a good agreement.

If we assume again a pressureless fluid as in the 2D case, if we additionally assume that $\partial \Phi_0 / \partial z \ll \partial \epsilon \Phi_1 / \partial z$ (which is of course a wrong assumption to make in the present case), and that

$$\epsilon u_{z,1}(R, \phi, z) = \text{Re} \left\{ u_z^a(R, z) e^{im(\phi - \Omega_p t)} \right\}, \quad (48)$$

the third of Euler's equation (without any reduction factor) to the first order in ϵ leads to (as first shown in Faure et al. 2014)

$$u_z^a(R, z) = i \frac{\partial \Phi_a(R, z) / \partial z}{m [\Omega(R) - \Omega_p]}. \quad (49)$$

We compare Eq. (49) with the predictions of Eq. (40) in Fig. 6. This comparison is made by averaging $u_z(R, \phi, z)$ over z with weight $\exp(-\nu^2 z^2 / 2\sigma_z^2)$ (i.e., in the case where the vertical density is isothermal like in the case of Schwarzschild's DF). The predictions of Eq. (49) are an order of magnitude larger than the predictions of Eq. (40) and the simulation (so much that we do not show, for readability, the complete range of Fig. 6). The phases are instead in perfect agreement. A more sophisticated (albeit not fully dynamical) approach was taken by Monari et al. (2015), relating the radial and tangential motions for a very cold stellar disc or fluid to the vertical motions via the continuity equation. The predictions of Monari et al. (2015) (again, averaged

along z with weight the isothermal density distribution) are also shown on Fig. 6, allowing to show the typical reduction factor (as well as some phase-shift related to missing terms in the cold fluid approximation). We note that the breathing modes are qualitatively similar to those observed in the extended solar neighbourhood (Williams et al. 2013), but that the amplitude of these motions is much lower than observed. It nevertheless remains to be seen how the coupling of multiple perturbers will affect these vertical motions (Monari et al. in prep.).

4.3 Distribution function at a point in configuration space

Our computation of the exact form of the perturbed DF away from the main resonances also allows us to study the detailed behaviour of $f = f_0 + \epsilon f_1$ at a given point in configuration space (R, ϕ, z) , in terms of the actions and angles, and compare it with the unperturbed version of the DF, f_0 . First, let us note that the dimensions of phase-space, given the constraint of a fixed point in configuration space, $(R, \phi, z) = \text{constant}$, decrease from 6 to 3, even when the DF depends both on actions *and* angles. We focus on the case $(R, \phi, z) = (8 \text{ kpc}, 0, 0)$ (i.e, the typical position of the Sun in our model) and we add the constraint $J_z = 0$, additionally decreasing the dimensionality of phase-space to 2 dimensions.

The two variables that we choose to display are (θ_R, J_R) . The other angles and actions are constrained by $R = R_g(J_\phi) - \sqrt{2J_R/\kappa(J_\phi)} \cos \theta_R$, $J_z = 0$, $\theta_\phi = \phi + \Delta\phi(J_\phi, J_R, \theta_R)$, and $\theta_z = \pi/2$ (because $z = 0$). In practice we solve numerically the first of this constraints for each pair (θ_R, J_R) to get J_ϕ , and it is then trivial to get θ_ϕ . In the case of the unperturbed DF, f_0 , the true dependence is obviously on J_R and J_ϕ , but we can translate it in terms of (θ_R, J_R) in terms of the above constraints at a fixed point in configuration space.

The comparison between $f_0(\theta_R, J_R)$ and $f(\theta_R, J_R)$ is shown in Fig. 7. As is apparent from this figure, both f_0 and f decrease with J_R , but f_0 is symmetric with respect to $\theta_R =$

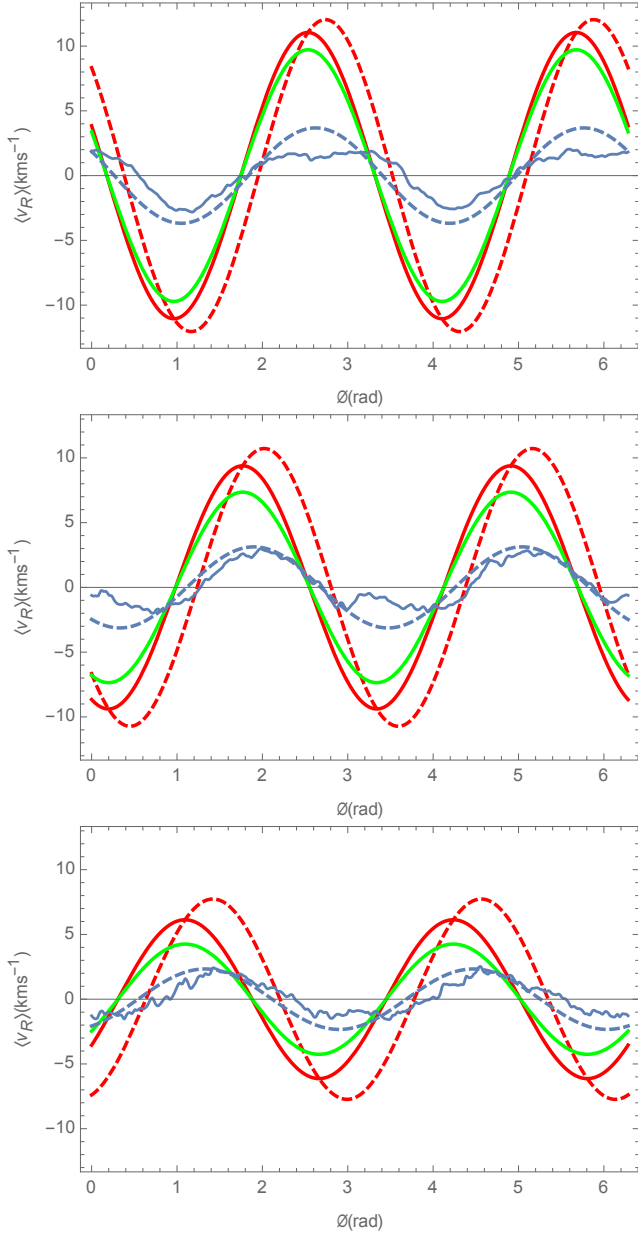


Figure 3. Several predictions for the response of mean v_R of a stellar system or a cold fluid to the potential model used in this work. Predictions by (predictions by Lin & Shu 1964, 1966; Lin et al. 1969): red dashed line Eq. (46), red solid line Eq. (47), green line Eq. (47) multiplied by the reduction factor \mathcal{F} by Binney & Tremaine 2008. Blue dashed line Eq. (39), blue solid line simulation. Top panel: $R = 7$ kpc. Central panel: $R = 8$ kpc. Bottom panel: $R = 9$ kpc.

π while f not, which is due to the $\exp(\pm i\theta_R)$ terms. The asymmetries in Fig. 7 can be directly translated to features in the (v_R, v_ϕ) velocity space. To visualize this transformation, we are helped by the map in Fig. 8, which shows how to associate (θ_R, J_R) with (v_R, v_ϕ) at $(R, \phi, z) = (8 \text{ kpc}, 0, 0)$. This figure displays curves of constant J_R and θ_R in the (v_R, v_ϕ) space (see also McMillan 2011). Each of the central circular curves represents a value of J_R , while the lines that radiate from $(v_R, v_\phi) = (0, 220 \text{ km s}^{-1})$ represent constant values of θ_R .

It is then interesting to check the behaviour of the velocity distribution function at such a particular point in space, i.e., $f(v_R, v_\phi, v_z)$ at constant (R, ϕ, z) , as we can e.g., compare it to the velocity of the stars in the Solar neighbourhood (the small volume around the Sun where, to date, detailed enough kinematic data are present). As a matter of fact, velocity-space substructures in the Solar neighbourhood, called *moving groups*, have observationally been shown to be composed of stars of different ages and chemical compositions (e.g. Dehnen 1998; Chereul et al. 1999; Famaey et al. 2005, 2008; Pompéia et al. 2011). For this reason, they are most likely associated to perturbations from the bar and spiral arms (e.g., Dehnen 2000; Minchev et al. 2010; Antoja et al. 2011; Quillen et al. 2011). Our model is based on a single spiral perturber, and is valid only away from the main resonances, so we do not expect the model to reproduce all the observed features. Nevertheless, it is interesting to look at the trend (note that the “Solar neighbourhood” in our model is indeed away from the main resonances as we chose parameters such that ILR = 1.56 kpc and CR = 11.49 kpc).

In Fig. 9 (top panel) we show the perturbed DF $f(v_R, v_\phi)$ at $(R, \phi, z) = (8 \text{ kpc}, 0, 0)$. We see how the effect of the perturbation is to deform the density contours so that the stars are not anymore distributed symmetrically between positive and negative v_R . In particular there is an excess of stars slightly lagging rotation and moving outwards around $v_R \simeq 30 \text{ km s}^{-1}$ and $v_\phi = 210 \text{ km s}^{-1}$. This particular configuration of the density contours is reminiscent of that created by the Hyades moving group in the Solar neighbourhood⁴. These features can be easily interpreted in light of Fig. 7 and Fig. 8. For example, fixing $J_R = 30 \text{ km s}^{-1} \text{ kpc}$ and moving clockwise from $\theta_R = 0$, we first encounter in Fig. 7 an underdensity at $\theta_R \approx \pi/5$. Then the density increases again at $\theta_R = \pi/2$, forming in Fig. 9 (top) the Hyades-like distortion. At $\theta_R \approx \pi$ it is almost constant, to slightly decrease again for $\theta_R > \pi$. The general velocity distribution is slightly skewed towards negative radial velocities. In the bottom panel of Fig. 9, we then also show $f(v_R, v_\phi)$ at $(R, \phi, z) = (6 \text{ kpc}, 0, 0)$. Here we find more stars that in the previous case at $v_\phi < 220 \text{ km s}^{-1}$. Moreover, the two configurations in the DFs of Fig. 9 explain why there is a net $\langle v_R \rangle < 0$ motion at $(R, \phi, z) = (8 \text{ kpc}, 0, 0)$ in the Galaxy, while $\langle v_R \rangle > 0$ at $(R, \phi) = (6 \text{ kpc}, 0, 0)$, due to the asymmetry of the general velocity distribution.

In Fig. 10 we now show $f(v_R, v_z)$ fixing $v_\phi = v_c(7.5 \text{ kpc})$ and $(R, \phi, z) = (7.5 \text{ kpc}, 0, 0.3 \text{ kpc})$ (top panel) and $v_\phi = v_c(9.5 \text{ kpc})$ and $(R, \phi, z) = (9.5 \text{ kpc}, 0, 0.3 \text{ kpc})$ (bottom panel), hence at $z = 0.3 \text{ kpc}$ height from the Galactic plane⁵. The former case has $\Delta\langle v_z \rangle < 0$ and $\langle v_R \rangle > 0$, while the latter $\Delta\langle v_z \rangle > 0$ and $\langle v_R \rangle < 0$. The consequence of the perturbation is a tilt of the velocity ellipsoid in the $v_R - v_z$ space, that has opposite sign in the two points. Such a tilt would be impossible, by construction, with the unperturbed f_0 distribution function which is plane-parallel, and has a similar amplitude of that found by studies of stars in the

⁴ However, it is likely that the Hyades moving group is a resonant feature (Sellwood 2010; Hahn et al. 2011; McMillan 2011, 2013), thereby not precisely reproduced by the present model.

⁵ To obtain the DFs at $z = -0.3 \text{ kpc}$ it is sufficient to flip v_z with $-v_z$.

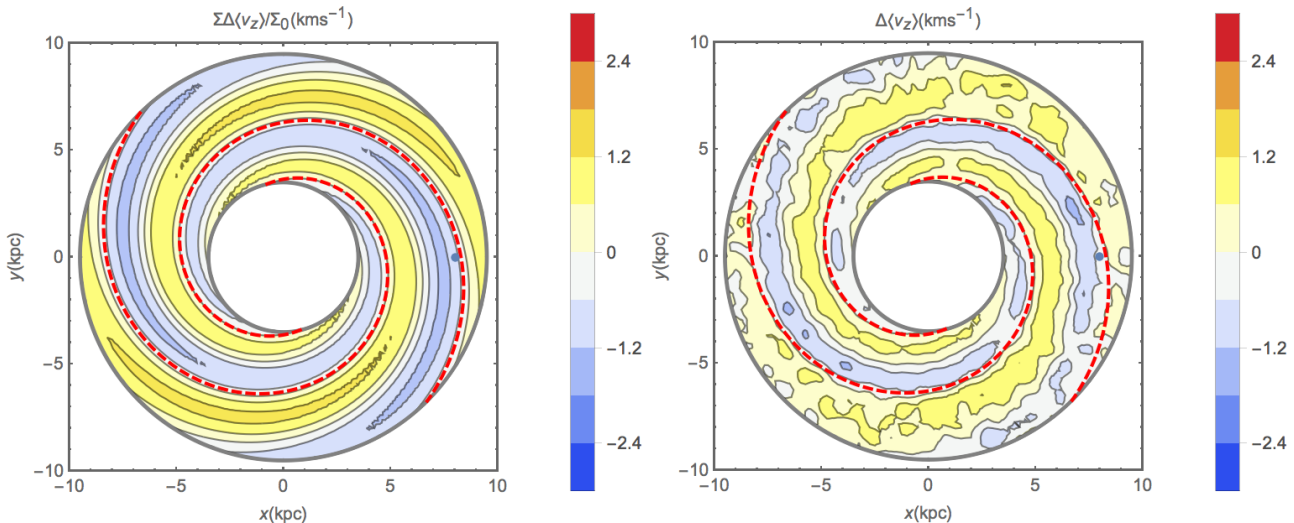


Figure 4. Mean v_z motions induced by the potential perturbation Eq. (43) on the Binney & Tremaine (2008) Model I potential. Left panel: north-south difference between the average vertical speed $\Sigma\Delta\langle v_z \rangle / \Sigma_0$ obtained from Eq. (40). Right panel: north-south difference between the average vertical speed computed from the simulation. For the simulation $\Delta\langle v_z \rangle$ is computed inside $x - y$ square bins of 0.25 kpc side, and smoothed with a Gaussian filter on a scale of 0.5 kpc. The dashed red curves represent the loci of the arms.

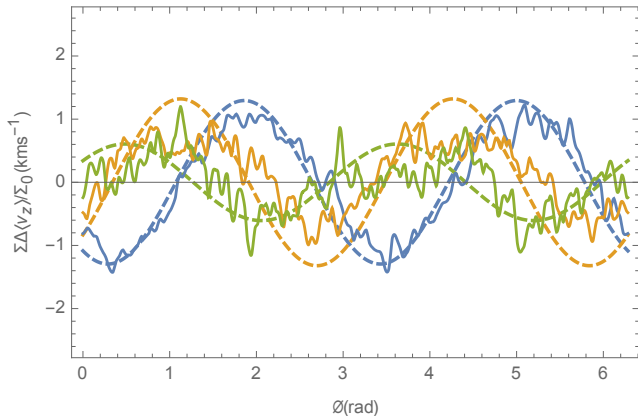


Figure 5. Comparison between the north-south difference in mean v_z motion $\Delta\langle v_z \rangle$ induced by the potential perturbation Eq. (43) on the Binney & Tremaine (2008) Model I potential as a function of ϕ at three different radii computed with a numerical test-particle simulation (solid lines) and Eq. (40) (dashed lines). Blue lines: $R = 7$ kpc. Orange lines: $R = 8$ kpc. Green lines: $R = 9$ kpc. The quantity for the simulation is computed inside $x - y$ square bins of 0.25 kpc side, smoothed with a Gaussian filter on a scale of 0.5 kpc, and polynomial interpolated on the $x - y$ grid.

Solar neighbourhood (e.g., Pasetto et al. 2012). The velocity ellipsoid is thus clearly influenced by the spiral potential, and this intuitively explains why there is a transition from positive to negative mean vertical motion precisely in between the arms and in the middle of the arms (where the mean radial motion is maximal), because the ellipsoid becomes plane-parallel again. Nevertheless, a tilt of the ellipsoid alone cannot cause a net vertical motion, as the average v_z would still be 0. But this tilt is actually accompanied by a lopsidedness of the v_z distribution, which is maximal when the tilt is maximal.

5 CONCLUSION AND PERSPECTIVES

This work presents a general way to calculate the effects of a non-axisymmetric gravitational disturbance on an axisymmetric DF, f_0 , describing the phase-space density of stars in a collisionless stellar system (i.e., governed by the collisionless Boltzmann equation). We assume that the axisymmetric f_0 alone solves the collisionless Boltzmann equation in an axisymmetric potential Φ_0 where the relationship between the ordinary positions and velocities and the action and angle variables are known (Section 2).

We apply this method to construct a 3D model of the Milky Way's thin disc, where the non-axisymmetric gravitational disturbance $\epsilon\Phi_1$ is a Fourier mode in azimuth (Section 3). In particular, we chose to describe bisymmetric spiral arms with a $\sim \text{sech}^2$ vertical falloff (Section 4.1). As a result, we obtain formulas for the DF and its zeroth and first order moments (density and mean motions) that are shown to be in agreement with a numerical test-particle simulation representing the effect of the same bisymmetric spiral arms on the Milky Way's thin disc (Section 4.2). In particular, we estimate for the first time the reduction factor for the vertical bulk motions of a stellar population compared to the case of a cold fluid.

An inspection of the DF at given points in 3D configuration space (Section 4.3) also helps to interpret these macroscopic properties of the stellar system. One interesting result is that the spiral arms induce a tilt and a lopsidedness in the $v_R - v_z$ velocity ellipsoid that changes of sign and magnitude as a function of the position of the point where it is calculated w.r.t. the spiral arms. In addition, it is shown that distortions typical of moving groups such as the Hyades are naturally reproduced in velocity space.

We nevertheless point out that our results here are only valid away from the main resonances. Indeed, our method consists in a linear treatment of the collisionless Boltzmann equation, i.e., it assumes that the non axisymmetric gravitational disturbance $\epsilon\Phi_1$ and DF response ϵf_1 are small.

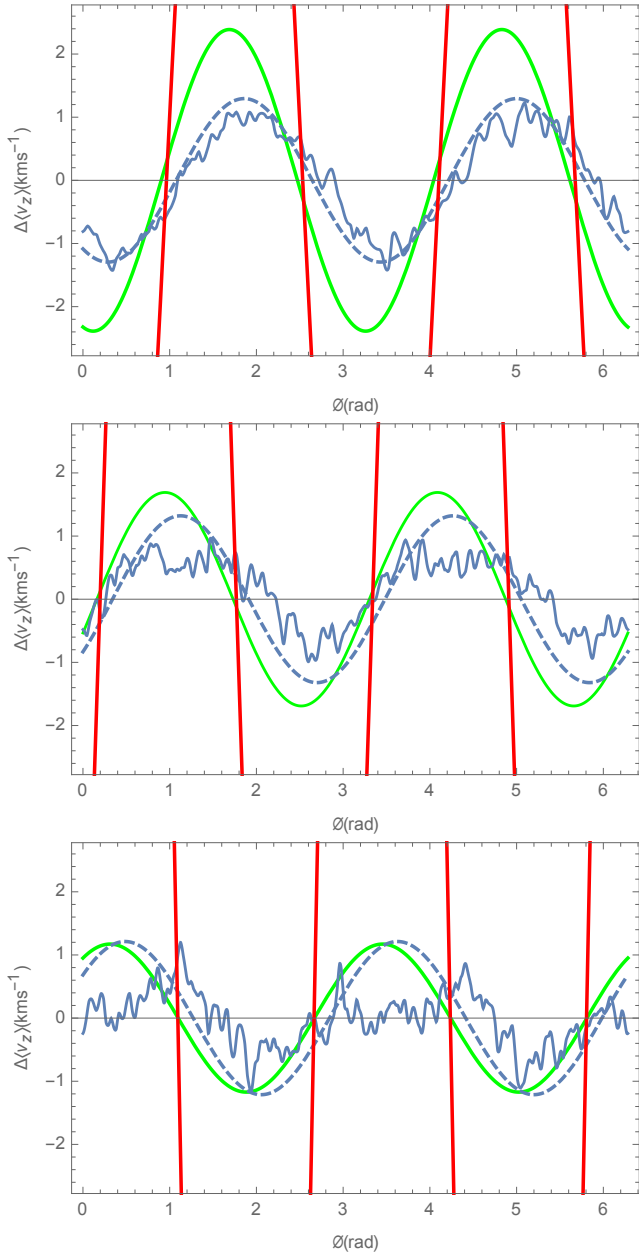


Figure 6. Several predictions for the response of mean v_z of a stellar system or a cold fluid to the potential model used in this work (red solid line Eq. (49), green line method by Monari et al. (2015) for a cold stellar disc, blue dashed line Eq. (40), blue solid line simulation). Top panel: $R = 7$ kpc. Central panel: $R = 8$ kpc. Bottom panel: $R = 9$ kpc.

In particular, f_0 should always be larger than ϵf_1 in order to preserve physical meaning. While most of the non-axisymmetric gravitational disturbances of the Milky Way are indeed much smaller than its background axisymmetric gravitational potential, certain regions of phase-space are particularly affected by the perturbations. These are the resonances, where the rotational, radial, and vertical frequencies and the perturbation pattern speed are commensurable. The linear regime breaks down at the resonances, as is evident from Eq. (30), whose denominator vanishes at the resonances. Even if there is an infinite number of reso-

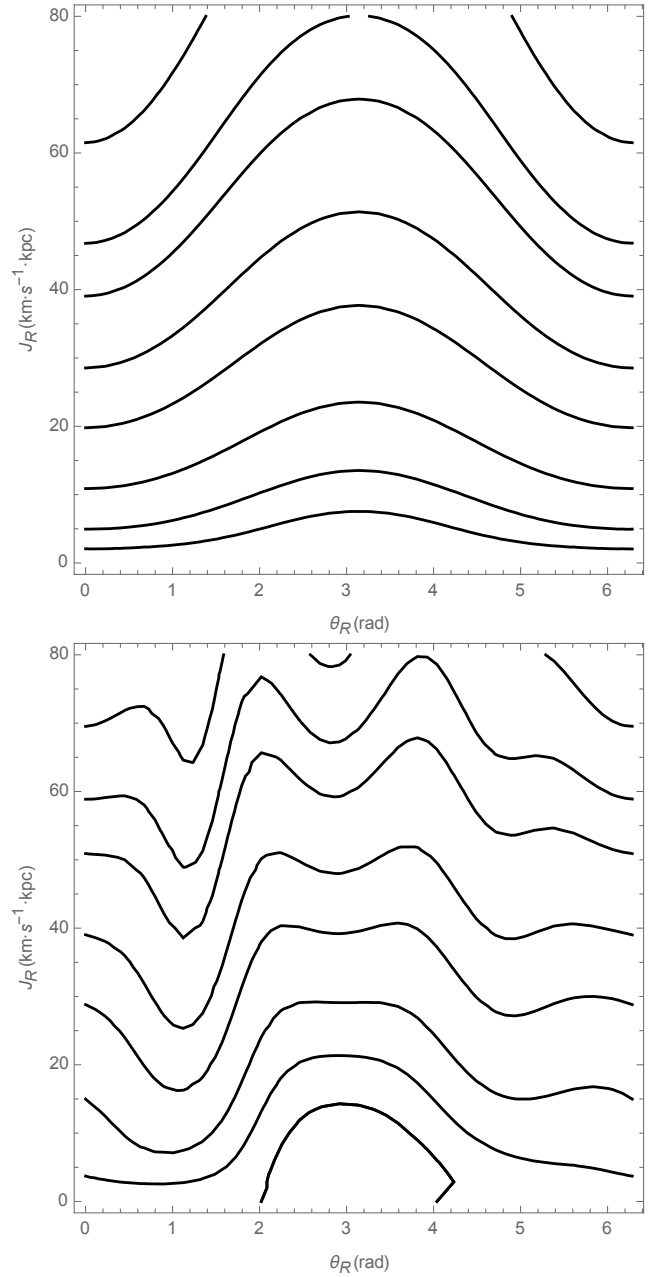


Figure 7. Isocontours of the distribution functions in the (θ_R, J_R) space at the point $(R, \phi, z) = (8 \text{ kpc}, 0, 0)$ of the Galactic plane. Top panel: $f_0(\theta_R, J_R)$. Bottom panel: $f(\theta_R, J_R)$. The contours enclose (from bottom to top) 12, 21, 33, 50, 68, 80, 90, 95, and 99% of the stars.

nances, those that affect a significant portion of phase-space are rare. In our treatment they appear for example at the corotation and Lindblad resonances that, in the case of the spiral arms we chose in this paper, are all quite far from the Solar neighbourhood. The same cannot be stated in the case of the bar, where the outer Lindblad resonance is probably close to the Sun. One way to treat the resonances that we will explore in forthcoming work is to pass, in their vicinity, to another system of angle-action variables (fast and slow variables), that allows to focus on the librations around the

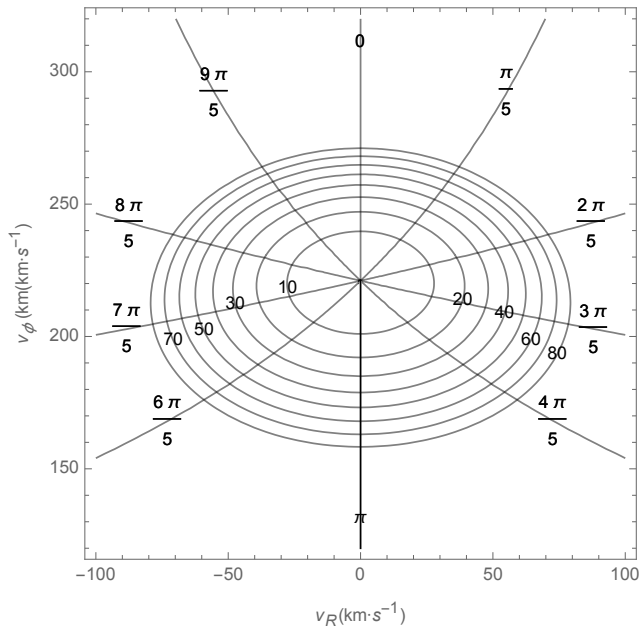


Figure 8. Curves of constant θ_R and J_R in velocity space at $(R, \phi, z) = (8 \text{ kpc}, 0, 0)$ for the Binney & Tremaine (2008) Model I potential. See also McMillan (2011).

resonant orbits, neglecting all the high frequency motions (see Binney & Tremaine 2008).

Another future issue, even more complex to treat, is related to the non-linear effects due to the presence of more than one perturber. In the linear perturbation theory presented here, the effect of more than one perturber would simply be the linear combination of the single responses. However, from numerical studies (Monari et al. in prep.), it can be shown that non-linear effects arise simply by superposing different perturbers, as the bar and spiral arms. This is especially important in terms of the amplitude of the vertical breathing mode generated by the spirals in this work, which is qualitatively similar to observations (Williams et al. 2013), but not quantitatively. The effect of multiple perturbers could be especially important in that case. Future analytic calculations should investigate this question. Also, in the present work, we concentrated on the response of a given disc stellar population in equilibrium to a perturbing three-dimensional spiral potential, but we did not investigate yet the conditions for self-consistency, which, especially in 3D, is a more complex problem than the present one, to be treated in the future too.

Finally, we note that, while we used the adiabatic and epicyclic approximations to estimate the angle and action variables in this work, the method to obtain the distribution function that we present at the beginning of the paper is completely general (Section 3.1). Our choice of using a Schwarzschild distribution function to represent the axisymmetric equilibrium configuration can trivially be generalized to other forms of the distribution function. Moreover, our results can also in principle be used with more sophisticated approximations of the angles and actions in the Milky Way potential already present in the literature. For this reason, the method presented in this paper will be helpful in the future to dynamically characterize the Milky Way disc stel-

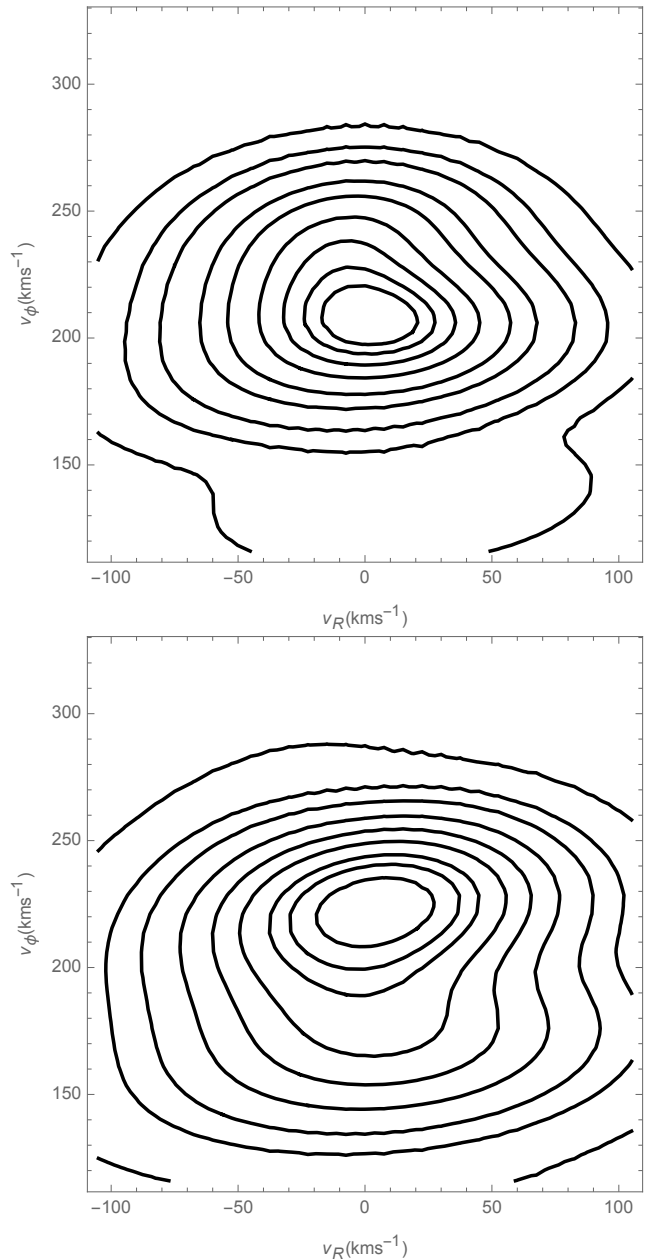


Figure 9. Isocontours of the velocity distribution functions $f(v_R, v_\phi)$ at two points of the Galactic plane. Top panel: $(R, \phi, z) = (8 \text{ kpc}, 0, 0)$. Bottom panel: $(R, \phi, z) = (6 \text{ kpc}, 0, 0)$. The contours enclose (from the inner to the outer) 12, 21, 33, 50, 68, 80, 90, 95, and 99% of the stars.

lar kinematic information that will be provided by upcoming large astrometric and spectroscopic surveys of the Galaxy, as it offers the possibility to interpret the latter in the dynamical sense (rather than just subtracting the residuals from a fiducial axisymmetric model), using a rather low number of free parameters.

ACKNOWLEDGEMENTS

This work has been supported by a postdoctoral grant from the *Centre National d'Etudes Spatiales* (CNES) for GM.

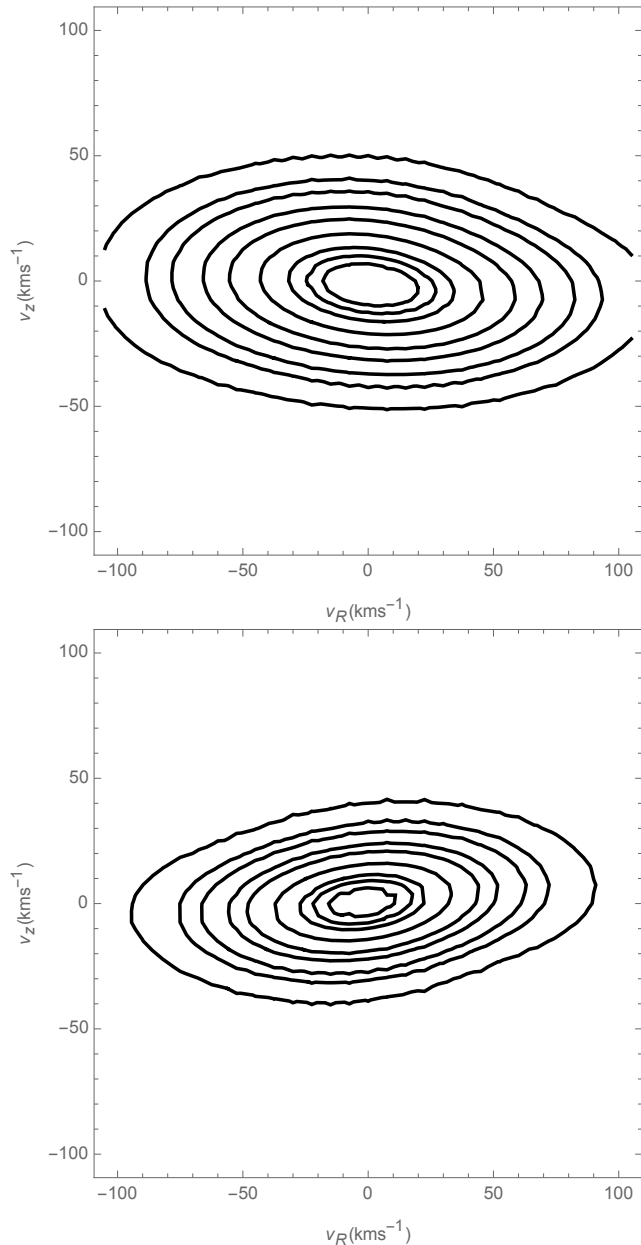


Figure 10. Isocontours of the velocity distribution functions $f(v_R, v_z)$ at two points at $z = 0.3$ kpc from the Galactic plane. Top panel: $(R, \phi, z) = (7.5 \text{ kpc}, 0, 0.3 \text{ kpc})$. Bottom panel: $(R, \phi, z) = (9.5 \text{ kpc}, 0, 0.3 \text{ kpc})$. The contours enclose (from the inner to the outer) 12, 21, 33, 50, 68, 80, 90, 95, and 99% of the stars.

REFERENCES

- Antoja T., Figueras F., Romero-Gómez M., Pichardo B., Valenzuela O., Moreno E., 2011, *MNRAS*, 418, 1423
- Bienaymé O., Robin A. C., Famaey B., 2015, *A&A*, 581, A123
- Binney J., 2010, *MNRAS*, 401, 2318
- Binney J., 2012, *MNRAS*, 426, 1324
- Binney J. et al., 2014, *MNRAS*, 439, 1231
- Binney J., Lacey C., 1988, *MNRAS*, 230, 597
- Binney J., McMillan P., 2011, *MNRAS*, 413, 1889
- Binney J., Piffl T., 2015, *MNRAS*, 454, 3653
- Binney J., Tremaine S., 2008, *Galactic Dynamics: Second Edition*, Binney, J. & Tremaine, S., ed. Princeton University Press
- Bovy J., Bird J. C., García Pérez A. E., Majewski S. R., Nidever D. L., Zasowski G., 2015, *ApJ*, 800, 83
- Bovy J., Rix H.-W., 2013, *ApJ*, 779, 115
- Carlberg R. G., 1987, in *Nearly Normal Galaxies. From the Planck Time to the Present*, Faber S. M., ed., pp. 129–137
- Carlberg R. G., Sellwood J. A., 1985, *ApJ*, 292, 79
- Carlin J. L. et al., 2013, *ApJ*, 777, L5
- Chereul E., Crézé M., Bienaymé O., 1999, *A&AS*, 135, 5
- Cox D. P., Gómez G. C., 2002, *ApJS*, 142, 261
- de la Vega A., Quillen A. C., Carlin J. L., Chakrabarti S., D’Onghia E., 2015, *MNRAS*, 454, 933
- Debattista V. P., 2014, *MNRAS*, 443, L1
- Dehnen W., 1998, *AJ*, 115, 2384
- Dehnen W., 1999, *ApJ*, 524, L35
- Dehnen W., 2000, *AJ*, 119, 800
- Dehnen W., Binney J., 1998, *MNRAS*, 294, 429
- Famaey B., Dejonghe H., 2003, *MNRAS*, 340, 752
- Famaey B., Jorissen A., Luri X., Mayor M., Udry S., Dejonghe H., Turon C., 2005, *A&A*, 430, 165
- Famaey B., Siebert A., Jorissen A., 2008, *A&A*, 483, 453
- Faure C., Siebert A., Famaey B., 2014, *MNRAS*, 440, 2564
- Feldmann R., Spolyar D., 2015, *MNRAS*, 446, 1000
- Fouvry J.-B., Binney J., Pichon C., 2015, *ApJ*, 806, 117
- Gómez F. A., Minchev I., O’Shea B. W., Beers T. C., Bullock J. S., Purcell C. W., 2013, *MNRAS*, 429, 159
- Gómez F. A., White S. D. M., Marinacci F., Slater C. T., Grand R. J. J., Springel V., Pakmor R., 2015, *ArXiv e-prints*
- Grand R. J. J., Bovy J., Kawata D., Hunt J. A. S., Famaey B., Siebert A., Monari G., Cropper M., 2015, *MNRAS*, 453, 1867
- Hahn C. H., Sellwood J. A., Pryor C., 2011, *MNRAS*, 418, 2459
- Kalnajns A. J., 1971, *ApJ*, 166, 275
- Lin C. C., Shu F. H., 1964, *ApJ*, 140, 646
- Lin C. C., Shu F. H., 1966, *Proceedings of the National Academy of Science*, 55, 229
- Lin C. C., Yuan C., Shu F. H., 1969, *ApJ*, 155, 721
- McGill C., Binney J., 1990, *MNRAS*, 244, 634
- McMillan P. J., 2011, *MNRAS*, 418, 1565
- McMillan P. J., 2013, *MNRAS*, 430, 3276
- McMillan P. J., Binney J. J., 2008, *MNRAS*, 390, 429
- Minchev I., Boily C., Siebert A., Bienaymé O., 2010, *MNRAS*, 407, 2122
- Minchev I. et al., 2014, *ApJ*, 781, L20
- Minchev I., Famaey B., 2010, *ApJ*, 722, 112
- Monari G., Famaey B., Siebert A., 2015, *MNRAS*, 452, 747
- Monari G., Helmi A., Antoja T., Steinmetz M., 2014, *A&A*, 569, A69
- Pasetto S. et al., 2012, *A&A*, 547, A71
- Piffl T., Penoyre Z., Binney J., 2015, *MNRAS*, 451, 639
- Pompéia L. et al., 2011, *MNRAS*, 415, 1138
- Prusti T., 2012, *Astronomische Nachrichten*, 333, 453
- Quillen A. C., 2003, *AJ*, 125, 785
- Quillen A. C., Dougherty J., Bagley M. B., Minchev I., Comarretta J., 2011, *MNRAS*, 417, 762
- Sanders J. L., Binney J., 2014, *MNRAS*, 441, 3284
- Schönrich R., 2012, *MNRAS*, 427, 274

- Schönrich R., Binney J., Dehnen W., 2010, MNRAS, 403, 1829
Sellwood J. A., 2010, MNRAS, 409, 145
Sellwood J. A., Carlberg R. G., 2014, ApJ, 785, 137
Siebert A. et al., 2012, MNRAS, 425, 2335
Siebert A. et al., 2011, MNRAS, 412, 2026
Weinberg M. D., 1994, ApJ, 420, 597
Widrow L. M., Barber J., Chequers M. H., Cheng E., 2014, MNRAS, 440, 1971
Widrow L. M., Gardner S., Yanny B., Dodelson S., Chen H.-Y., 2012, ApJ, 750, L41
Williams M. E. K. et al., 2013, MNRAS, 436, 101
Xu Y., Newberg H. J., Carlin J. L., Liu C., Deng L., Li J., Schönrich R., Yanny B., 2015, ApJ, 801, 105
Yanny B., Gardner S., 2013, ApJ, 777, 91